ORIGINAL ARTICLE

Computing Volume Potentials for Noninvasive Imaging of Cardiac Excitation

A.W. Maurits van der Graaf, M.D.,* Pranav Bhagirath, M.D.,* Vincent J.H.M. van Driel, M.D.,* Hemanth Ramanna, M.D., Ph.D.,* Jacques de Hooge, M.Sc.,* Natasja M.S. de Groot, M.D., Ph.D.,† and Marco J.W. Götte, M.D., Ph.D.*

*From the *Department of Cardiology, Haga Teaching Hospital, The Hague, The Netherlands. and †Department of Cardiology, Erasmus Medical Center, Rotterdam, The Netherlands*

Background: In noninvasive imaging of cardiac excitation, the use of body surface potentials (BSP) rather than body volume potentials (BVP) has been favored due to enhanced computational efficiency and reduced modeling effort. Nowadays, increased computational power and the availability of open source software enable the calculation of BVP for clinical purposes. In order to illustrate the possible advantages of this approach, the explanatory power of BVP is investigated using a rectangular tank filled with an electrolytic conductor and a patient specific three dimensional model.

Methods: MRI images of the tank and of a patient were obtained in three orthogonal directions using a turbo spin echo MRI sequence. MRI images were segmented in three dimensional using custom written software. Gmsh software was used for mesh generation. BVP were computed using a transfer matrix and FEniCS software.

Results: The solution for 240,000 nodes, corresponding to a resolution of 5 mm throughout the thorax volume, was computed in 3 minutes. The tank experiment revealed that an increased electrode surface renders the position of the 4 V equipotential plane insensitive to mesh cell size and reduces simulated deviations. In the patient-specific model, the impact of assigning a different conductivity to lung tissue on the distribution of volume potentials could be visualized.

Conclusion: Generation of high quality volume meshes and computation of BVP with a resolution of 5 mm is feasible using generally available software and hardware. Estimation of BVP may lead to an improved understanding of the genesis of BSP and sources of local inaccuracies.

Ann Noninvasive Electrocardiol 2014;00(0):1–8

electrocardiography; noninvasive imaging of cardiac excitation; finite element method; inverse procedure

Noninvasive imaging of cardiac excitation using recorded body surface potentials (BSP) and mathematical inverse procedures is an active field of research that has yielded some clinical applications.[1–4] In an inverse procedure, local epicardial potentials or myocardial activation times are computed from recorded BSP. In contrast, a forward procedure estimates BSP from potentials measured on the surface of the heart.[5,6]

The boundary element method (BEM) has been favored for electrocardiographic forward procedures due to enhanced computational efficiency and reduced modeling effort.[7–9] In contrast to the BEM, which yields potential information on predefined surfaces, the finite element method (FEM) provides body volume potentials (BVP; Fig. 1).[10] Utilizing knowledge on the spatial potential field may lead to improved insight in the potential distribution throughout the thorax. Although potentials can be computed everywhere in a volume as well using the BEM by creating multiple surfaces inside the volume, the FEM is

Address for correspondence: A.W.M. van der Graaf, M.D., Haga Teaching Hospital, Department of Cardiology, Leyweg 275, 2545 CH The Hague, The Netherlands. Fax: 0031 70 210 2224; E-mail: a.vandergraaf@hagaziekenhuis.nl

Disclosures: our institution has received research grants from St Jude Medical and Medtronic NL. None of the authors report a potential conflict of interest.

DOI:10.1111/anec.12183

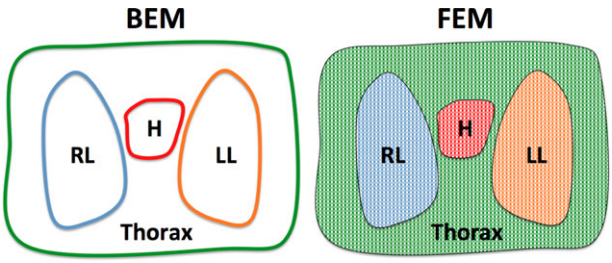

Figure 1. The boundary element method (BEM) yields potential information on predefined surfaces only. Hence, no information on the areas between the compartments can be derived when using the BEM. The finite element method (FEM) on the contrary, provides BVP. Volume potentials can be computed as well using the BEM, by increasing the number of model compartments. However, the FEM is typically more efficient, especially when the number of model compartments is high or when anisotropic conductivity is modeled. RL = right lung; LL = left lung; H = heart; L = liver.

typically more efficient for this purpose. Especially when the number of model compartments is high or when anisotropic conductivity is modeled, the FEM is recommended.[11]

Although the application of BVP has been studied previously,[12,13] it has never advanced into clinical practice due to its time consuming and elaborative nature. Increased computational power and the introduction of open source software enable the calculation of BVP for clinical purposes. In this study, the explanatory power of BVP is illustrated by experiments performed in a simple rectangular tank. In addition, simulations in a three dimensional patient specific model demonstrate the possible advantage of using BVP.

METHODS

Rectangular Tank

A rectangular tank of 33 × 25 × 25 cm filled with an electrolytic conductor was used. Electrodes with a surface of 2 × 2 cm were positioned in the middle of opposing sides. To block interference from nearby power sources, a 1000 Hz 8 V peak-to-peak sinusoidal power source was used. Measurements were performed using a dual beam oscilloscope, enabling monitoring of the source voltage while measuring the resulting potential in the tank. The accuracy of the measurements approximated 2%, which was considered sufficient for validation purposes.

MRI Images

MRI images of the rectangular tank and the patient were acquired using a turbo spin echo (black blood) sequence in three orthogonal directions (slice thickness 8mm). Electrode positions in the tank and on the body surface were marked using liquid-filled vitamin D capsules, appearing hyperintense on MRI. The MRI scan was performed on a Siemens Aera 1.5 Tesla MRI scanner (Siemens Healthcare, Erlangen, Germany).

The study complied with the declaration of Helsinki and received approval from the local ethical committee and the institutional scientific board. Written informed consent was obtained from the patient.

Meshing

In order to achieve topological propriety, MRI images were segmented in three dimensions using bounding planes. No spatial smoothing was applied. The Gmsh tool,[14] freely available on the Internet for noncommercial use, was used for mesh generation.

Computing BVP

Given the source potential distribution on the epicardial surface, the resulting volume potential distribution is governed by the equations below.

The current density J as a function of conductivity s and field strength E is given by ohms law:

$$J = sE = s\,\mathrm{grad}(P), \text{ where P is the potential.} \quad (1)$$

Apart from the heart there are no current sources in the thorax so:

$$\mathrm{div}(J) == 0. \quad (2)$$

From (1) and (2) follows Laplace's equation:

$$\mathrm{div}(s\,\mathrm{grad}(P)) == 0. \quad (3)$$

Multiplying by a test function T leads to the following variational form:

$$\int \mathrm{div}(s\,\mathrm{grad}(P))T\,dV == \int 0 * T\,dV == 0. \quad (4)$$

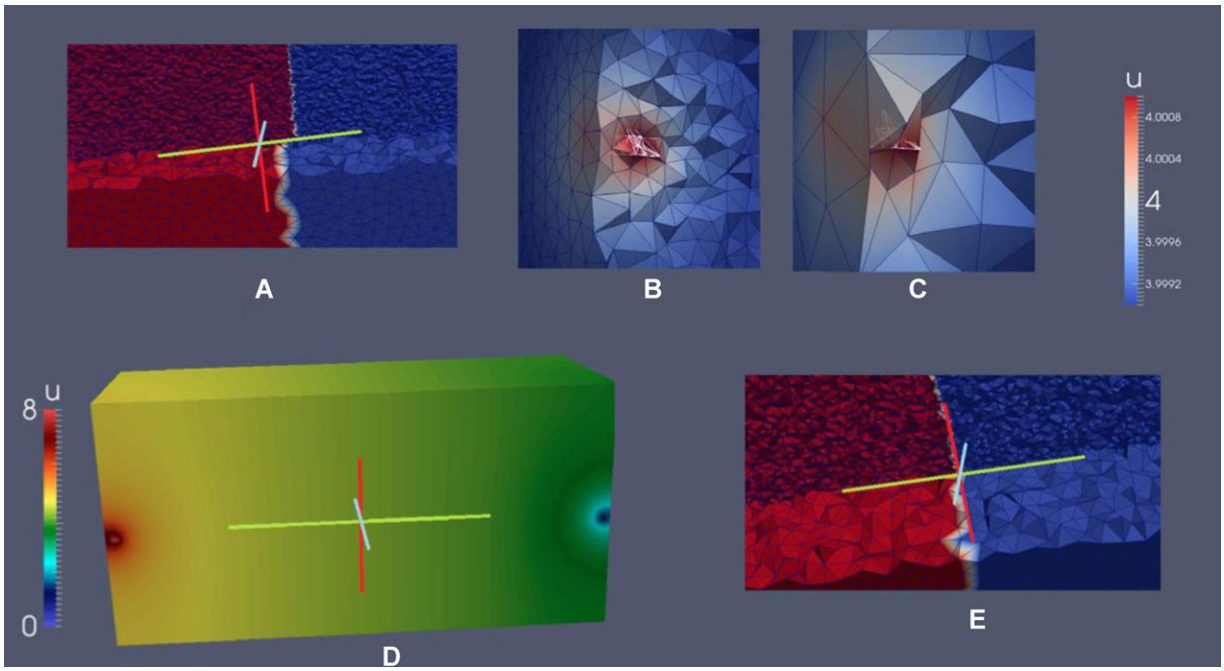

Figure 2. (A) Using a tetrahedral mesh with an edge length of 1.5 cm computed position of the 4 V equipotential plane (white) deviates from the measured position that was in the middle of the tank. Refining the mesh to an edge length of 0.5 cm increases the deviation. A large potential drop was observed in the vicinity of positive electrode, which is indicated by the white wireframe, both for the fine (B) and the crude (C) grid. Artifacts depend on the exact location of the grid cells with respect to the electrodes, which may be coincidentally more asymmetric with the fine grid. (D) In the middle of the tank, the x coordinate (green axis) varies rapidly as a function of the potential. (E) Large electrodes render the position of the 4 V equipotential plane insensitive to the mesh cell size at the same time decreasing the deviation from the middle.

Partial integration yields (n is the unit surface normal):

$$\int \text{div}(s\ \text{grad}(P)\ T\ dV = = \int s\ \text{grad}(P).\text{grad}(T)\ dV - \int s\ \text{grad}(P).n\ T\ dS. \quad (5)$$

From (4) and (5) follows:

$$\int s\ \text{grad}(P).\text{grad}(T)\ dV == \int s\ \text{grad}(P).n\ T\ dS. \quad (6)$$

With J.n = 0 and (1) at the skin this becomes:

$$\int s\ \text{grad}(P).\text{grad}(T)\ dV = 0. \quad (7)$$

To yield a nontrivial solution, the source potentials at the heart surface are applied as boundary conditions. There are many general-purpose FEM tools available to solve these equations. FEniCS,[15] freely available for research purposes, was selected.

This software package allowed the aforementioned equation to be specified in a very natural form. All work is done by the following lines of code:

```
RHS = sigma*inner(grad(trialFunction),grad
  (testFunction)) * dx (1)
LHS = Constant (0)* testFunction * dx (2)
A,b = assemble_system(LHS,RHS,boundaryCond,
  keep_diagonal = True) (3)
solve(A,potential.vector(),b,'gmres','
  default') (4)
```

Note the close correspondence between lines [1] and [2] of the code and Equation (6) by substituting them in equation LHS = RHS.

Computing Platform

All analyses were performed on a 2.4 GHz quadcore laptop running Windows 8 OS. Solving the potential equations was delegated to a an Ubuntu 12.10 virtual machine running on this laptop, communicating with the activation modeling

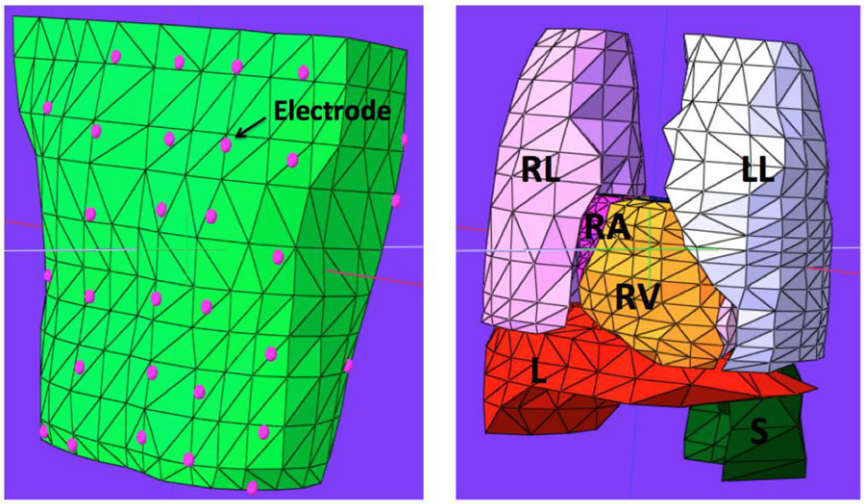

Figure 3. A three dimensional computer model of the human thorax with the positions of the body surface electrodes (A). The electrode positions were derived from the positions of the liquid-filled vitamin D capsules, appearing hyperintense on MRI. The thorax model contains multiple compartments (B). RA = right atrium; RV = right ventricle; S = spleen.

software by the use of synchronized message file sharing. Reference times were computed using a single core.

RESULTS

Rectangular Tank

Figure 2 shows the three dimensional mesh of the tank. A potential of 4 V peak to peak was observed in the middle of the tank. The computations using a tetrahedral mesh with 1.5 cm edge length, demonstrated a deviation of the 4 V plane from the middle by about one grid cell. By refining the mesh to an edge length of 0.5 cm, this deviation was expected to diminish. Paradoxically, the deviation from the middle actually increased by about 2.5 cm, to a total deviation about 10 times larger than the mesh size (Fig. 2A).

Figure 2B and C reveal the potential gradients to increase near to the electrode. This is caused by the small contact area between the fluid and the electrodes introducing a high resistivity: R = 1/(area × sigma) (Ohm/m). Because R is large, the potential drop U is large according to Ohms law. Moreover, a relative misrepresentation of the electrode area by 5% leads to a relative error in this potential drop in the same order of magnitude.

Figure 2(D) illustrates that minor errors in the potential drop near the electrodes yield large deviations in the 4 V equipotential plane. In the middle of the tank the x coordinate varies rapidly with small potential changes. By using volume information, the counterintuitive effect shown in Figure 2A can be understood. For large electrodes, misrepresentations of their area by the mesh are relatively small. This should render the position of the 4 V equipotential plane insensitive to the mesh cell size (Fig. 2E).

Patient Torso

Figure 3 shows a multicompartment three dimensional computer model of a human thorax. The positions of the electrodes on the body surface were derived from the anatomic markers on MRI. Figure 4 demonstrates the resulting three dimensional mesh. As can be observed the mesh is highly regular and is locally refined in the vicinity of details.

Shortest Paths of Activation

The computation of all possible shortest paths of the activation wavefront through the cardiac wall resulted in a set of epicardial isochrones yielding

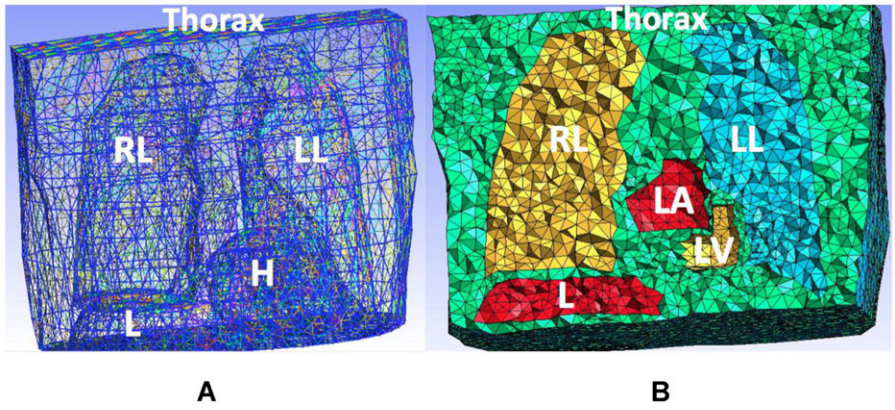

Figure 4. Locally refined multicompartment thorax three dimensional mesh (A) and volume mesh (B). The mesh is error free and was generated in 25 seconds using freely available software on a 2.4 GHz single core on a laptop. No spatial smoothing was applied. LA = left atrium; LV = left ventricle.

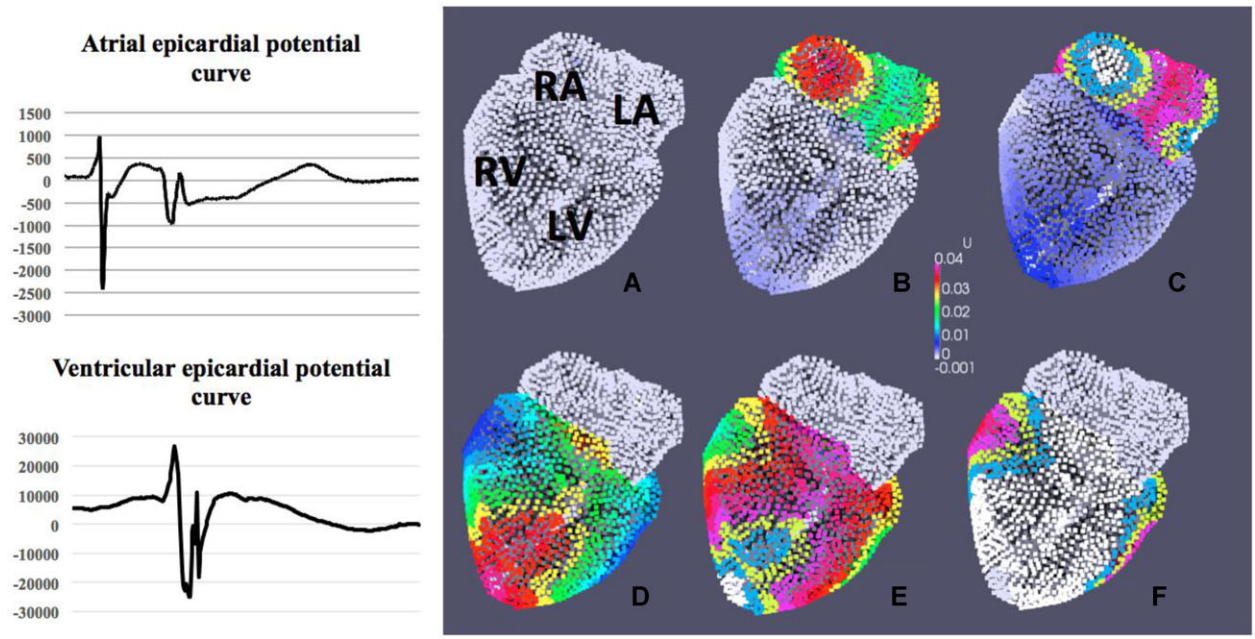

Figure 5. Snapshots of the time-dependent epicardial potential, taken from a sequence of 50 time steps. On the left, an example of atrial (top) and ventricular (bottom) epicardial potentials is displayed.

a time dependent epicardial potential as shown in Figure 5.

Computing BVP

Potential equations for 13,000 mesh nodes were solved in 3 seconds utilizing a 2.4 GHz single core. Solving these equations for a mesh consisting of 240,000 nodes, corresponding to a resolution of 5 mm throughout the thorax volume, lasted 3 minutes. Two sequences of computed BVP are shown in Figure 6, one using a mesh edge size of 0.5 cm (A–J) and one using a mesh edge size of 1.5 cm (K–T). The potential field permeates the lungs without visual deformation, even if their sigma is only half that of their environment.

Impact of Lung Tissue on BVP

The impact of variable organ conductivity on BVP was investigated using forward simulations in the human torso model. Figure 7 illustrates

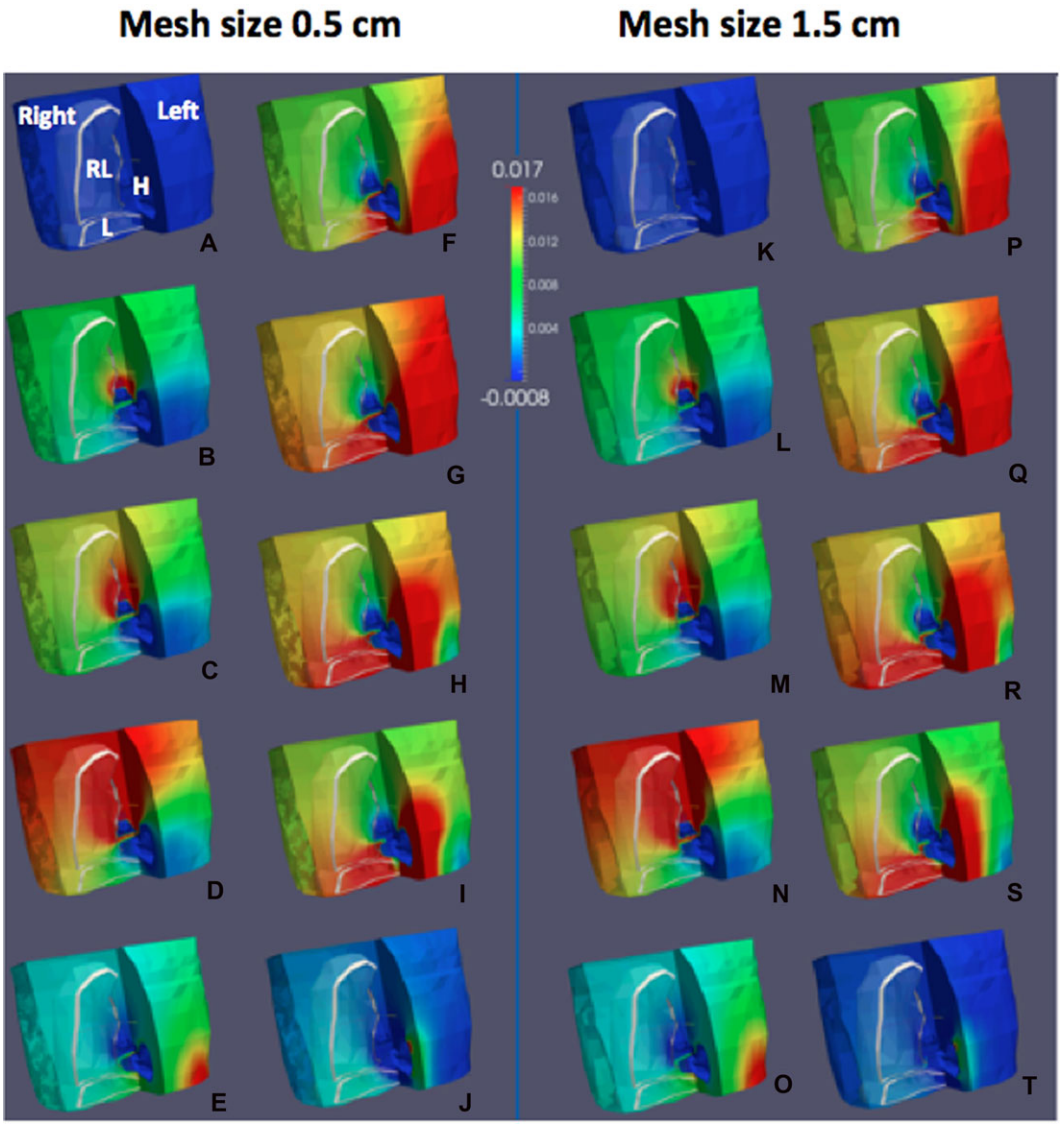

Figure 6. Frontal view of the thorax. Shown are the computed BVP during one heartbeat. (A–J) Mesh edge size is 0.5 cm. (K–T) Mesh edge size is 1.5 cm. The crude edges are artifacts from segmentation, performed in three dimensional. Since topology had to be preserved, no spatial smoothing was applied.

the impact on the electric field when a smaller sigma (conductivity) is assigned to lung tissue (A). The BVP field is compared to simulations in a homogeneous torso model (B). A smaller sigma of the lung tissue leads to an increased breakthrough of the potential field.

DISCUSSION

In this study the feasibility of computing BVP for noninvasive imaging of cardiac excitation is illustrated. So far, volume potentials have been considered to be of limited value. However, computing BVP using the FEM is efficient if the number of bounding surfaces between organs taken into account is high. In addition, using the FEM rather than the BEM enables the incorporation of different anisotropies, local tissue characteristics and sigma gradients over different regions. BVP may be used to gain a better insight in the genesis of BSP and sources of local inaccuracies.

Figure 6 suggests that the computed BVP hardly depend on the mesh cell characteristic length for a

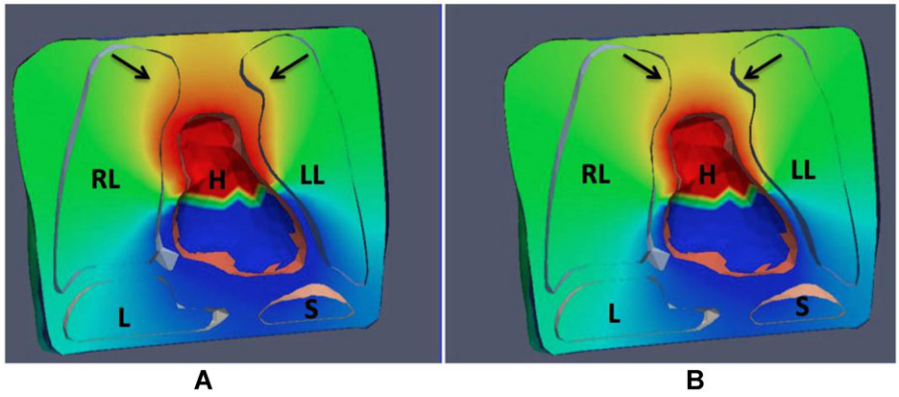

Figure 7. The impact of variable organ conductivity on BVP. A smaller sigma of the lung tissue leads to an increased breakthrough of the potential field (A), compared to simulations in a homogeneous torso model (B).

ratio as big as 1:3. However, the tank experiment indicates that there are geometries where the mesh size does have a significant influence on the outcome. The FEM could be used to understand which aspects of the geometry caused the large misrepresentation of the 4 V equipotential plane. By visualizing the large potential gradient near the electrodes and the small potential gradient in the middle of the box, the FEM contributed to understanding the inaccuracy of the computed position of the 4 V equipotential plane.

Computation of BVP

From a computational standpoint, computing a potential field by means of the FEM is not a problem. The computation time of a 240,000 points potential field was approximately 3 minutes. Graphics processors with hundreds of computation units combined with quadcore main CPUs are becoming available at consumer prices. Generally available FEM packages are able to benefit from this just by setting some parameters and no custom coding. While the performance gain by computing the FEM in parallel may easily be 10-fold. The FEniCS package has been selected because this tool has a lot of mindshare, a vivid user community and excellent documentation.

Meshing

Generating high quality meshes and solving differential equations have been part of engineering disciplines for decades. In many articles on biomedical computing, generation of a computational mesh is taken for granted. Early experiments revealed that generation of a surface mesh from a labeled voxel set often leads to irregular meshes with topological errors that are hard to repair. Several groups have developed their own meshing software and others have proposed to do away with meshing altogether.[16–18] However, the meshing itself does not appear to be the problem. General-purpose mesh generation tools can generate high quality volume meshes in a matter of seconds for an arbitrarily complex segmentation result, provided that the segmentation contains no topological errors.

Fast generation of volume meshes and FEM solutions with generally available means has brought computation of BVP as part of noninvasive imaging of cardiac excitation within practical clinical reach. This route will further be explored, hoping to gain direct and visual insight in the sources of inaccuracies, including the so called "ill conditioning" of the inverse problem, in the required number of electrodes, numbers of less than 20 to more than 200 currently being advocated in literature,[19,20] and in the optimal placement of these electrodes in individual patients.

CONCLUSION

This study illustrates that efficient generation of high quality volume meshes and computation of BVP with a resolution of 5 mm is feasible using generally available software and hardware. With the computational effort decreasing dramatically, estimation of BVP may be seasonable when the number of model compartments is high or when anisotropic conductivity is modeled. Observing

the potential field everywhere in the thorax may lead to an improved understanding of the genesis of BSP and sources of local inaccuracies. In the near future, computation of BVP for noninvasive imaging of cardiac excitation may evolve toward clinical application.

Acknowledgment: *Our institution has received research grants from St Jude Medical and Medtronic NL. These sponsors did not have any involvement in the research discussed in this article.*

REFERENCES

1. Desouza KA, Joseph SM, Cuculich PS, et al. Noninvasive mapping of ventricular activation in patients with transplanted hearts.J Electrocardiol 2013;46(6):698–701.
2. Sapp JL, Dawoud F, Clements JC, et al. Inverse solution mapping of epicardial potentials: quantitative comparison with epicardial contact mapping. Circ Arrhythm Electrophysiol 2012;5(5):1001–1009
3. Galeotti L, van Dam PM, Loring Z, et al. Evaluating strict and conventional left bundle branch block criteria using electrocardiographic simulations. Europace 2013;15(12):1816–1821.
4. Berger T, Pfeifer B, Hanser FF, et al. Single-beat noninvasive imaging of ventricular endocardial and epicardial activation in patients undergoing CRT. PLoS One 2011;27;6(1):e16255.
5. Gulrajani RM. The forward and inverse problems of electrocardiography. IEEE Eng Med Biol Mag 1998;17(5):84–101.
6. van der Graaf AW, Bhagirath P, Ramanna H, et al. Noninvasive imaging of cardiac excitation: Current status and future perspective.Ann Noninvasive Electrocardiol 2014;19(2):105–113.
7. Stenroos M, Haueisen J. Boundary element computations in the forward and inverse problems of electrocardiography: comparison of collocation and Galerkin weightings.IEEE Trans Biomed Eng 2008;55(9):2124–2133.
8. Wang Y, Rudy Y. Application of the method of fundamental solutions to potential-based inverse electrocardiography. Ann Biomed Eng 2006;34(8):1272–1288.
9. Van Dam PM, Oostendorp TF, Linnenbank AC, et al. Noninvasive imaging of cardiac activation and recovery.Ann Biomed Eng 2009;37(9):1739–1756.
10. Hunter P. FEM/BEM notes. *CMISS* Auckland Bioengineering Institute and Engineering Science. New Zealand, The University of Auckland, 2008:1–140.
11. Shahidi AV, Savard P, Nadeau R. Forward and inverse problems of electrocardiography: modeling and recovery of epicardial potentials in humans.IEEE Trans Biomed Eng 1994;41(3):249–256.
12. Klepfer RN, Johnson CR, Macleod RS. The effects of inhomogeneities and anisotropies on electrocardiographic fields: A 3-D finite-element study.IEEE Trans Biomed Eng 1997;44(8):706–719.
13. Wang D, Kirby RM, Macleod RS, Johnson CR. Inverse electrocardiographic source localization of ischemia: an optimization framework and finite element solution.J Comput Phys 2013;1(250):403–424.
14. Marchandise E, Geuzaine C, Remacle JF. Cardiovascular and lung mesh generation based on centerlines.Int J Numer Method Biomed Eng 2013;29(6):665–682.
15. Kekenes-Huskey PM, Gillette A, Hake J, McCammon JA. Finite element estimation of protein-ligand association rates with post-encounter effects: Applications to calcium binding in Troponin C and SERCA. Comput Sci Discov. 2012 Oct 31;5. pii: 014015.
16. Wang Y, Rudy Y. Meshless methods in potential inverse electrocardiography. Conf Proc IEEE Eng Med Biol Soc 2006;1:2558–2559.
17. Li ZS, Zhu SA, He B. Solving the ECG forward problem by means of a meshless finite element method. Phys Med Biol 2007;52(13):N287–296.
18. Chinchapatnam P, Rhode K, Ginks M, Nair PB, Razavi R, Arridge SR, Sermesant M. Voxel based adaptive meshless method for cardiac electrophysiology simulation. Lecture Notes in Computer Science 2009;5528:182–190.
19. Rudy Y. Noninvasive electrocardiographic imaging of arrhythmogenic substrates in humans.Circ Res 2013;112(5):863–874.
20. Van Dam PM, Tung R, Shivkumar K, Laks M. Quantitative localization of premature ventricular contractions using myocardial activation ECGI from the standard 12-lead electrocardiogram. J Electrocardiol 2013;46(6): 574–579.